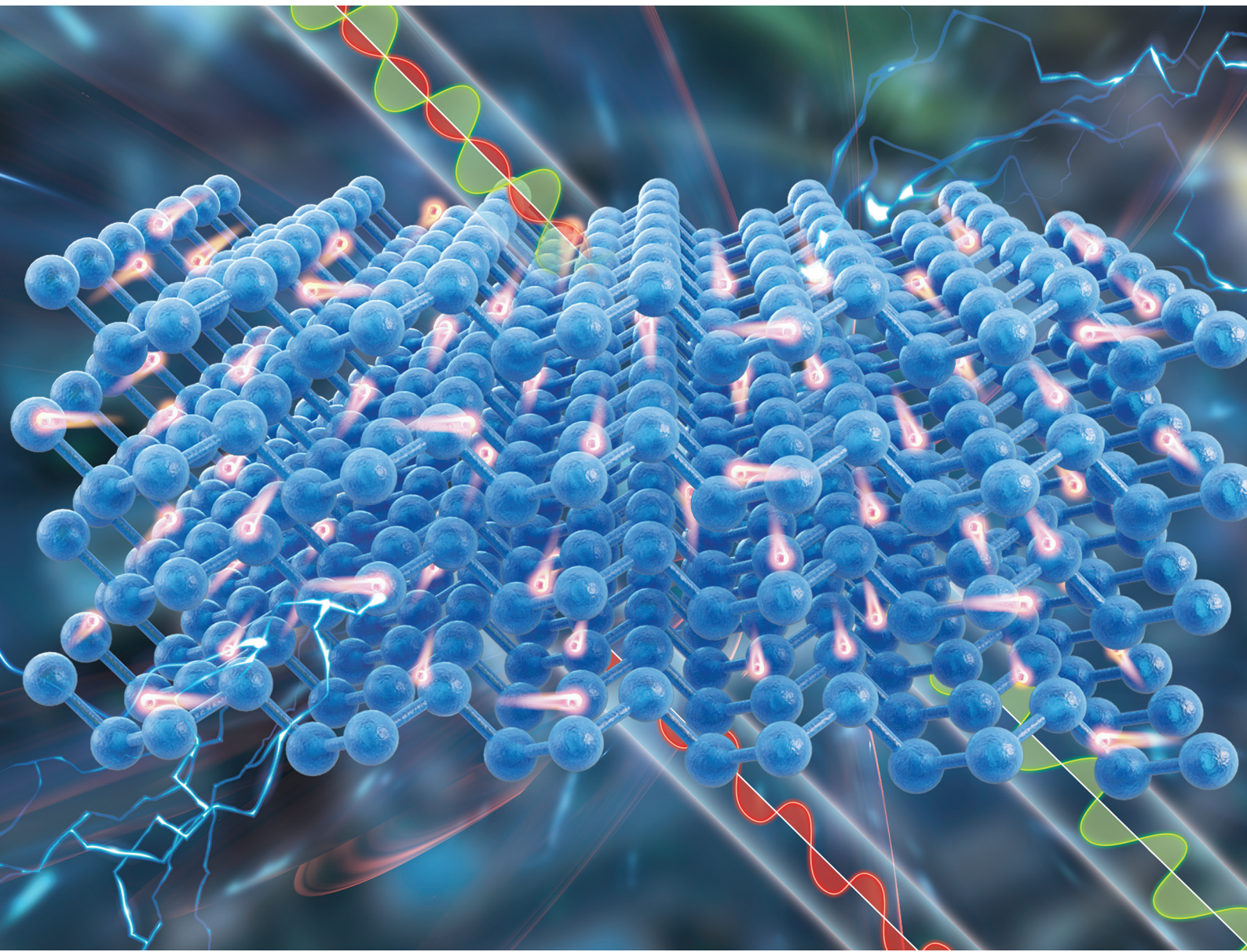


Nanoscale

rsc.li/nanoscale



ISSN 2040-3372



Cite this: *Nanoscale*, 2022, **14**, 12238

Giant in-plane optical and electronic anisotropy of tellurene: a quantitative exploration†

Zhengfeng Guo, ^{a,b} Honggang Gu, *^{a,c} Mingsheng Fang, ^a Lei Ye^d and Shiyuan Liu *^{a,c,d}

Tellurene's giant in-plane optical anisotropy brings richer physics and an extra degree of freedom to regulate its optical properties for designing novel and unique polarization-sensitive devices. Here, we quantitatively evaluate the in-plane optical anisotropy of tellurene and further reveal its physical origins by combining imaging Mueller matrix spectroscopic ellipsometry (MMSE) and first-principles calculations. The anisotropic complex refractive indices and dielectric functions, as well as the derived giant birefringence ($|\Delta n|_{\max} = 0.48$) and dichroism ($\Delta k > 0.4$), are accurately determined by imaging MMSE to quantitatively evaluate the in-plane optical anisotropy of tellurene. With density functional theory (DFT), tellurene's optical anisotropy is connected to its low-symmetry lattice structure with electrical anisotropy (including the anisotropic effective mass, partial charge density, and carrier mobility), leading to anisotropic electric polarization and ultimately optical anisotropy. This work provides a general and quantitative way to explore the optical anisotropy and also helps to comprehend the connection between the lattice structure and the optical anisotropy of tellurene and even other emerging low-symmetry materials, which will further promote their polarization-sensitive optical applications.

Received 11th June 2022,

Accepted 26th July 2022

DOI: 10.1039/d2nr03226k

rsc.li/nanoscale

Introduction

As an elementary two-dimensional (2D) material, 2D tellurene exhibits abundant and appealing properties, such as high carrier mobility ($\sim 700\text{--}900\text{ cm}^2\text{ s}^{-1}\text{ V}^{-1}$),^{1,2} thickness tunable bandgaps,³ chirality,^{4,5} Weyl semiconductive properties,⁶ etc.⁷ More attractively, compared with the materials with out-of-plane optical anisotropy such as graphene,⁸ MoS₂,⁹ h-BN,¹⁰ etc., tellurene exhibits more accessible in-plane optical anisotropy, which is demonstrated by polarization-resolved reflectance and transmission spectroscopy,¹¹ angle-resolved polarized Raman spectroscopy,^{1,2} polarization imaging,² etc. Besides, the in-plane optical anisotropy will bring much richer physics, such as dichroism¹² and birefringence,^{13,14} and add an extra degree of (in-plane) freedom to regulate the

intrinsic optical properties for novel polarization-sensitive applications,^{15–17} which cannot be realized by isotropic and even out-of-plane optically anisotropic materials. However, much research attention has been paid to the qualitative observation and discussion of the optical anisotropic phenomena of tellurene, and the literature on quantitatively evaluating optical anisotropy and further revealing its relationship with the low-symmetry lattice structure is nearly absent.

Optical functions, including complex refractive indices and dielectric functions, represent the response of materials to the light and reflect the intrinsic light-matter interactions,^{18–20} such as interband transition,^{21,22} excitonic effect,^{23,24} etc. For low-symmetry materials, anisotropic optical functions can be used to quantitatively evaluate and modulate the optically anisotropic phenomena. For example, the reflectance of bulk materials along different crystal axes can be calculated directly from the anisotropic complex refractive indices.¹⁹ The anisotropic dielectric functions, reflecting the response of the anisotropic carrier behaviors to light, connect the electronic anisotropy with the optical anisotropy and help to reveal the relationship between the optical anisotropy and the low-symmetry lattice structure.

Herein, we quantitatively reveal the strong in-plane optical anisotropy of tellurene with high-accuracy and high-reliability optical constants by imaging Mueller matrix spectroscopic ellipsometry (MMSE) and dig deep into the relationship between the low-symmetry lattice structure and the optical an-

^aState Key Laboratory of Digital Manufacturing Equipment and Technology, Huazhong University of Science and Technology, Wuhan 430074, China.

E-mail: hongganggu@hust.edu.cn, shyliu@hust.edu.cn

^bInnovation Institute, Huazhong University of Science and Technology, Wuhan 430074, China

^cOptics Valley Laboratory, Wuhan 430074, China

^dSchool of Optical and Electronic Information, Huazhong University of Science and Technology, Wuhan 430074, China

†Electronic supplementary information (ESI) available: Details of Raman measurement and calculations, imaging Mueller matrix spectroscopic ellipsometry measurement and analysis, comparison of birefringence, and electrical anisotropy calculations. See DOI: <https://doi.org/10.1039/d2nr03226k>

isotropy with the help of electronic anisotropy. The low-symmetry lattice structure of the tellurene nanosheet is confirmed by Raman spectroscopy at first. The azimuth-sensitive Mueller matrix off-diagonal element spectra, polarization-resolved reflectance spectra, and angle-resolved Raman spectra are then applied to qualitatively observe and discuss highly in-plane anisotropic phenomena in the optics of the Te single crystal sample and tellurene. Furthermore, the optical constant and the dielectric function of tellurene, determined by imaging MMSE, quantitatively reveal the giant in-plane optical anisotropy. The highly in-plane optical anisotropy is also quantitatively revealed by the giant birefringence and dichroism of tellurene. Finally, the highly in-plane electronic anisotropy in effective mass, partial charge density, and carrier mobility is introduced to bridge the connection between tellurene's low-symmetry lattice structure and its optical anisotropy.

Results and discussion

Low-symmetry lattice structure

Tellurene is an untypical 2D material, and Fig. 1a–c illustrate its low-symmetry lattice structure. As shown in Fig. 1a and c, the van der Waals (vdW) interaction exists among adjacent helical chains composed of covalently bonded Te atoms^{1,25} instead of interlayers like other 2D materials.²⁶ Besides, these helical chains lie in the layer of tellurene as illustrated in Fig. 1b. Therefore, the high-order rotation axis and the optical axis lie in the layer of tellurene.²⁵ Different from the other uniaxial crystals with out-of-plane optical anisotropy such as graphene,⁸ MoS₂,⁹ h-BN,¹⁰ etc., whose optical axis is perpendicular to the layer, the optical axis lying in the layer of tellurene is the origin of in-plane optical anisotropy.

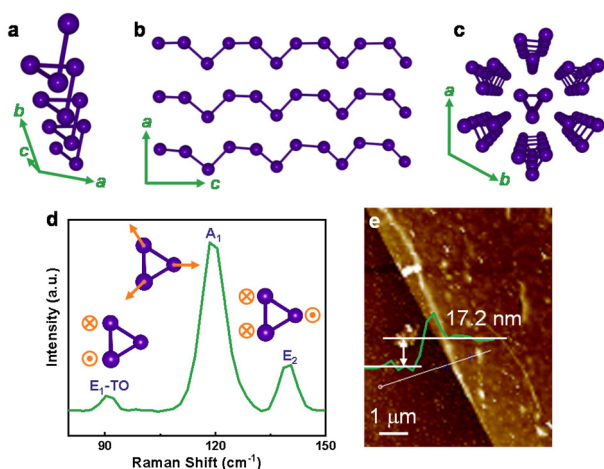


Fig. 1 Low-symmetry lattice structure and morphology of the tellurene nanosheet. (a–c) Schematics of the lattice structure with different views. (d) Raman spectrum and the corresponding lattice vibration modes (insets). (e) The atomic force microscopy (AFM) image of the tellurene nanosheet with a thickness of 17.2 nm.

The low-symmetry lattice structure of tellurene is confirmed from the Raman spectrum as given in Fig. 1d. Three peaks located at 90, 118, and 141 cm⁻¹ can be identified in the spectrum, corresponding to the E₁-TO, A₁ and E₂ Raman modes, respectively. These results are in great accord with the previous literature.^{1,2,27} As shown in the inset of Fig. 1d, each Raman mode represents the specific lattice vibration modes, and therefore confirms the low-symmetry lattice structure of tellurene. Specifically, the E₁-TO mode is the transverse phonon of the E₁ mode, which is attributed to the bond-bending along the *a*-axis,²⁸ and the E₂ mode is assigned to the asymmetric stretching mainly along the *c*-axis.^{27,29} The A₁ mode is the chain expansion mode in which each atom moves in the basal plane.²⁹ Besides, the typical nanosheet morphology of tellurene is characterized by atomic force microscopy (AFM) with a thickness of 17.2 nm.

In-plane optical anisotropy

The azimuth-dependent Mueller matrix spectra of the tellurium (Te) single crystal are measured by MMSE to confirm the presence of in-plane optical anisotropy in Te. As is known, the off-diagonal Mueller matrix elements are sensitive to the in-plane optical anisotropy of materials, and they will diverge from zero and vary with the rotation of the optical axis in plane.^{30,31} One can observe from Fig. 2a that the normalized off-diagonal Mueller matrix element M_{41} , the second row and the fourth column of the Mueller matrix, reaches a relatively high absolute value of about 0.3 at a wavelength of 285 nm, indicating that the measured sample possesses giant in-plane optical anisotropy. In the experiments, the sample was rotated in the *i*-*j* plane of ellipsometric measurement coordinates (*i*-*j*-*k*) to achieve azimuth-dependent results as shown in Fig. S1 of the ESI.† Since the optical axis of tellurene lies in the *i*-*j* plane, changing the azimuth is equivalent to rotating the optical axis in plane. Fig. 2b more clearly demonstrates the variation of M_{24} with the azimuth at a wavelength of 285 nm. The long side direction (*i.e.*, the *c*-axis), parallel to the direction of the optical axis, of the sample is placed to be parallel to the incident plane, which means that the azimuth is set to be zero, at the beginning of the ellipsometric measurement. As shown in Fig. S1,† when the optical axis is parallel or vertical to the incident plane, the sample appears to be “isotropic” in the measured Mueller matrix. Consequently, M_{24} is zero at the azimuths of 0° (or 180°) and 90° (or 270°) in Fig. 2b. It can also be observed from Fig. 2b that M_{41} exhibits a sinusoid-like curve *versus* the azimuth. The value of M_{24} immensely varies *versus* the azimuth from 0° to 360°, convincingly proving that the variation of in-plane optical anisotropy is caused by the optical axis of Te rotating in plane. Other off-diagonal elements, such as M_{13} , M_{24} , and M_{32} , show similar variation curves with M_{41} as shown in Fig. S2,† which further confirms the in-plane optical anisotropy in Te.

As we care more about 2D tellurene, angle-resolved polarized Raman spectroscopy is adopted to observe and discuss the in-plane optical anisotropy in the tellurene nanosheet. As shown in Fig. S3,† the polarizer and analyzer are parallel to

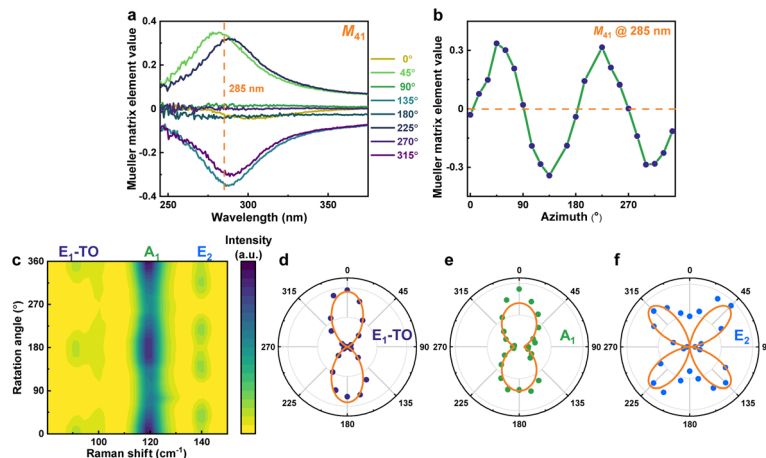


Fig. 2 In-plane optical anisotropies in the tellurium and tellurene nanosheets. (a) Measured spectra for the off-diagonal Mueller matrix element M_{41} of the tellurium single crystal at different azimuths. (b) Variation curve of M_{41} versus the azimuth at a wavelength of 285 nm. (c) Contour color map of the angle-resolved Raman spectra of the tellurene nanosheet. (d–f) Polar plots of the measured (solid dots) and calculated (solid lines) peak intensities of the $E_1\text{-TO}$, A_1 , and E_2 Raman modes, respectively.

each other in the Raman measurement system, and the tellurene nanosheet is anticlockwise rotated in the x - z plane of Raman laboratory coordinates (x - y - z). Fig. 2c illustrates that the peak intensities of three Raman modes ($E_1\text{-TO}$, A_1 , and E_2) vary with the rotation angle of the tellurene nanosheet. One can tell two-lobe shapes for both the $E_1\text{-TO}$ peak and A_1 peak and a four-lobe shape for the E_2 peak in the polar coordinate curves as given in Fig. 2d–f, which are consistent with previous reports.^{1,2} We also calculate the peak intensities I of the A_1 , $E_1\text{-TO}$, and E_2 Raman modes in theory, which can be respectively expressed as^{32,33}

$$I_{A_1} \propto |a \sin^2(\theta + \alpha) + b \cos^2(\theta + \alpha)|^2, \quad (1a)$$

$$I_{E_1\text{-TO}} \propto |c \sin^2(\theta + \alpha)|^2, \quad (1b)$$

and

$$I_{E_2} \propto |-2d \sin(\theta + \alpha) \cos(\theta + \alpha)|^2 = |d \sin 2(\theta + \alpha)|^2. \quad (1c)$$

Here, θ and α are respectively the angle between the z -axis and the c -axis of the tellurene nanosheet and the rotation angle as shown in Fig. S4.† More details can be found in S1 of the ESI.† It can be seen from Fig. 2d–f that the theoretical calculated peak intensities of the Raman modes agree well with the experimental ones.

Quantitative evaluation of the optical anisotropy

To quantitatively investigate the optical anisotropy, high-resolution imaging MMSE is utilized to obtain the anisotropic optical constants of the tellurene nanosheet. In general, the optical constants refer to the complex refractive index $N = n + ik$, including the refractive index n and extinction coefficient k . The working principle of imaging MMSE is schematically shown in Fig. S5.† which consists of a rotating compensator on the source arm and a rotating analyzer on the detection

arm respectively, and is capable of measuring the first three rows of the Mueller matrix.³⁴ Combined with a microscopic imaging system, imaging MMSE has a high resolution of 2 μm ,³⁵ which is suitable for measuring micro-distributed samples such as novel 2D materials.

Fig. 3 shows the Mueller matrix images of the tellurene nanosheet measured by imaging MMSE at a wavelength of 405 nm. The tellurene nanosheet can be clearly recognized with a high contrast to the SiO_2/Si substrate even for the off-diagonal Mueller matrix elements, such as M_{13} and M_{24} . The high contrast in the Mueller matrix image confirms the high resolution of imaging MMSE and the strong optical anisotropy in the tellurene nanosheet. To extract the optical constants, a

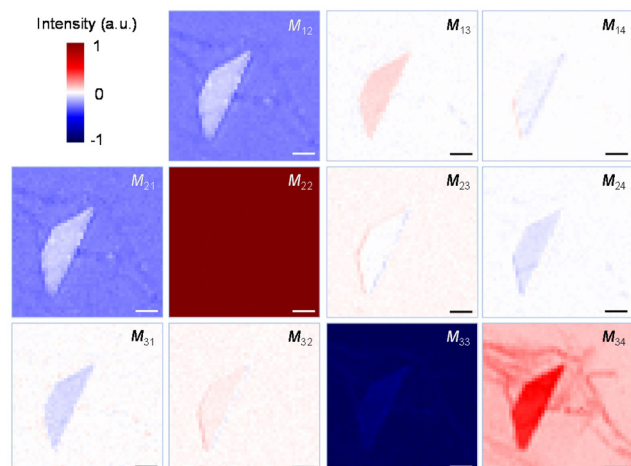


Fig. 3 The spatially resolved Mueller matrix images of the tellurene nanosheet at a wavelength of 405 nm measured by imaging MMSE at an incident angle of 45°, where the scale bar is 10 μm .

representative region in the tellurene nanosheet, *i.e.*, the triangle in the AFM image in Fig. S6,[†] is selected to perform the ellipsometric analysis.

In the ellipsometric analysis, a stacking model is constructed to optically describe the sample to calculate the theoretical Mueller matrix spectra (solid lines in Fig. S7[†]), which are used to fit the measured data (green points in Fig. S7[†]) to extract parameters, including the anisotropic dielectric functions and thickness of the sample.^{8,20,30} For the tellurene sample, the stacking model is the tellurene nanosheet and Si substrate with a SiO_2 oxide layer. More details about the ellipsometric analysis can be found in S2 in the ESI.[†] The theoretically calculated Mueller matrix spectra are in good agreement with the experimental ones as shown in Fig. S7[†]. The root-mean-square error (RMSE) is introduced to evaluate the fitness between the theoretical and measured Mueller matrix spectra, which is defined as^{8,30}

$$\text{RMSE} = \sqrt{\frac{1}{11L-p} \sum_{l=1}^L \sum_{i=1}^3 \sum_{j=1}^4 \left(M_{ij}^c - M_{ij}^m \right)^2} \times 1000. \quad (2)$$

Herein, L and p respectively denote the total spectral points and the number of fitting parameters, and l refers to the l -th point of the measured spectra. M_{ij}^c and M_{ij}^m are the calculated and measured Mueller matrix elements respectively, where subscripts i and j respectively refer to the i -th row and the j -th column of the Mueller matrix. The RMSE of the ellipsometric fitting is 10.4, which is at a relatively high level for a reliable ellipsometric analysis with a well-constructed optical model.

Since tellurene is a typical uniaxial crystal, the anisotropic dielectric functions can be described in a 3×3 diagonal tensor as given by

$$\begin{bmatrix} \epsilon_o & 0 & 0 \\ 0 & \epsilon_o & 0 \\ 0 & 0 & \epsilon_e \end{bmatrix} = \begin{bmatrix} \epsilon_{r,o} + i\epsilon_{i,o} & 0 & 0 \\ 0 & \epsilon_{r,o} + i\epsilon_{i,o} & 0 \\ 0 & 0 & \epsilon_{r,e} + i\epsilon_{i,e} \end{bmatrix}. \quad (3)$$

Herein, subscripts o and e respectively represent the directions vertical and parallel to the optical axis; ϵ_r and ϵ_i are respectively the real and imaginary parts of the dielectric function ϵ . Fig. 4a shows the measured anisotropic dielectric functions. It can be seen that the real parts of the dielectric functions along the optical axis $\epsilon_{r,e}$ and across the optical axis $\epsilon_{r,o}$ exhibit intense differences over the whole energy range (1.38–3.10 eV), displaying highly in-plane anisotropic features. Additionally, both $\epsilon_{r,e}$ and $\epsilon_{r,o}$ are below zero over most of the measurement energy ranges, confirming the metal-like behaviour of tellurene.³⁶ Since Te is a metalloid element, chemically non-metallic semiconductor Te can still conduct electricity like metals.³⁷ Compared with other chalcogens, such as S and Se, the nucleus attraction of Te is relatively weak, leading to the delocalization of Te lone-pair electrons like metals.³⁸ The first-principles calculated dielectric function spectra shown in Fig. S8a[†] also show such anisotropy and metal-like behaviour.

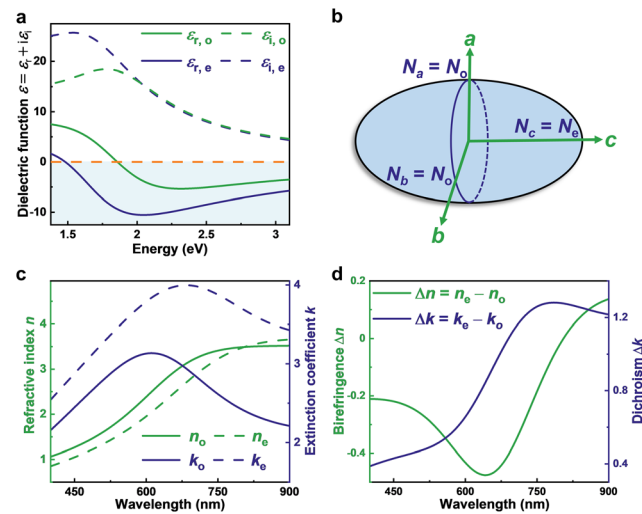


Fig. 4 Anisotropic complex refractive index and dielectric functions of the tellurene nanosheet. (a) Imaging MMSE measured dielectric function spectra. (b) The complex refractive index ellipsoid of the tellurene nanosheet. (c) Imaging MMSE measured complex refractive index spectra, including the refractive index and extinction coefficient. (d) The in-plane birefringence $\Delta n (= n_e - n_o)$ and dichroism $\Delta k (= k_e - k_o)$.

The complex refractive indices can be directly converted from the dielectric functions according to the following relations⁸

$$\begin{bmatrix} N_o^2 & 0 & 0 \\ 0 & N_o^2 & 0 \\ 0 & 0 & N_e^2 \end{bmatrix} = \begin{bmatrix} \epsilon_o & 0 & 0 \\ 0 & \epsilon_o & 0 \\ 0 & 0 & \epsilon_e \end{bmatrix}, \quad (4a)$$

$$\begin{bmatrix} (n_o + ik_o)^2 & 0 & 0 \\ 0 & (n_o + ik_o)^2 & 0 \\ 0 & 0 & (n_e + ik_e)^2 \end{bmatrix} = \begin{bmatrix} \epsilon_{r,o} + i\epsilon_{i,o} & 0 & 0 \\ 0 & \epsilon_{r,o} + i\epsilon_{i,o} & 0 \\ 0 & 0 & \epsilon_{r,e} + i\epsilon_{i,e} \end{bmatrix}. \quad (4b)$$

It can be seen from the complex refractive index ellipsoid in Fig. 4b that N_e is the complex refractive index along the direction of the optical axis (*i.e.*, $N_e = N_c$) while N_o is the complex refractive index along the a -axis and the b -axis (*i.e.*, $N_o = N_a = N_b$). It can be found from Fig. 4c that the measured spectra of both the refractive index and the extinction coefficient show distinct differences in the peak intensity and wavelength along the directions vertical and parallel to the optical axis, indicating that tellurene exhibits both giant birefringence and dichroism. Due to the optical anisotropy, although both the refractive index n and extinction coefficient k show a similar shape in the range of measurement wavelengths, n_o and k_o do not “catch up with” n_e and k_e respectively. The imaging MMSE measured complex refractive index also matches well with the calculated one (Fig. S8b[†]) with the help of first-principles calculations in the aspect of shapes of peaks, similarly illustrating

giant optical anisotropy leading to giant birefringence and dichroism.

The birefringence $\Delta n (= n_e - n_o)$ and the dichroism $\Delta k (= k_e - k_o)$ are further calculated to quantitatively evaluate the giant in-plane optical anisotropy of the tellurene nanosheet. It can be observed from Fig. 4d that the tellurene nanosheet exhibits negative birefringence at a relatively high level over the whole concerned spectral range, which coincides with the first-principles calculated one in Fig. S8c.[†] The maximum absolute birefringence $|\Delta n|_{\max}$ is 0.48 measured at a wavelength of 640 nm, which is higher than those of most commercial birefringent crystals (*e.g.*, quartz³⁹ and MgF_2 ⁴⁰), other low-dimensional materials (*e.g.*, black phosphorus⁴¹ and TiS_3 ⁴²), and representative well-designed birefringent materials^{43,44} as summarized in Table S2.[†] The tellurene nanosheet also maintains rather high positive dichroism ($\Delta k > 0.4$) over the whole concerned spectral range as shown in both Fig. 4d and Fig. S8c,[†] and the measured maximum reaches 1.38 at a wavelength of 785 nm. The giant measured and calculated birefringence and dichroism make the tellurene nanosheet a promising candidate for designing polarization-sensitive optoelectronic devices, such as wave plates,^{45,46} polarization-sensitive photodetectors,^{47,48} etc. We also investigated the thickness dependence of Δn and Δk with the help of first-principles calculations, as shown in Fig. S9.[†] The birefringence Δn in Fig. S9a[†] demonstrates an increasing tendency with the thickness of tellurene increasing, which is consistent with the fact that the bulk's Δn is usually larger than that of the 2D one.⁴⁹ In Fig. S9b,[†] Δk increases when the tellurene nanosheet becomes thicker at a relatively short wavelength, and with the increase of the wavelength, different layers of tellurene's Δk all approach zero.

Revealing the relationship between the low-symmetry lattice structure and the optical anisotropy

To further investigate the physical origin of the optical anisotropy more thoroughly, in-plane electronic anisotropy is introduced to bridge a connection between the low-symmetry lattice structure of the tellurene nanosheet and the optical anisotropy. Here, the electronic band structure and carrier mobility of the tellurene nanosheet are calculated by the first-principles method. Fig. 5a shows the electronic band structure of the tellurene nanosheet along a specific direction in the Brillouin zone, which can reflect the electronically anisotropic behaviours.^{50,51} One can find from the asymmetrically electronic band structure in Fig. 5b that both the valence and conduction bands along Γ -X (parallel to the *a*-axis of the tellurene nanosheet) display significant differences in the evolving slopes and band curvatures compared to those along Γ -Y (parallel to the *c*-axis, *i.e.*, the optical axis of the tellurene nanosheet). To quantitatively explain the anisotropy in the electronic band structure, the effective masses of the valence band maximum (VBM) and conduction band minimum (CBM) along Γ -X and Γ -Y in the Brillouin zone are calculated by

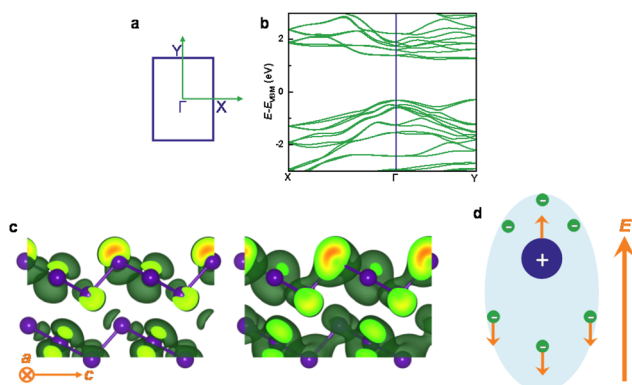


Fig. 5 Electronic anisotropy in the tellurene nanosheet. (a) The Brillouin zone of the tellurene nanosheet. (b) First-principles calculated band structure along Γ -X and Γ -Y. (c) The charge density of the valence band maximum (VBM) using an isosurface of $0.3 \text{ me } \text{\AA}^{-3}$, left: along the *a*-axis; right: along the *c*-axis. (d) Schematic of the electric polarization.

using the second order derivative of the CBM and VBM, as expressed by⁵²

$$m_{ij}^* = \frac{\partial^2 E_i}{\partial k_j^2} (i = e, h; j = a, c). \quad (5)$$

In eqn (5), subscripts *i* (*e*, *h*) and *j* (*a*, *c*) respectively represent the carrier type (electron, hole) and crystal axis (*a*-axis, *c*-axis) of the tellurene nanosheet. As shown in Table 1, the effective masses of the electron and hole along the *a*-axis manifest obvious differences from those along the *c*-axis. In particular, the effective mass of the electron along the *a*-axis ($m_{e,a}^*$) is much greater than that along the *c*-axis ($m_{e,c}^*$), and the ratio of $m_{e,a}^*$ to $m_{e,c}^*$ reaches up to 4.33. The high differences in the effective masses of the electron and hole along and across the optical axis demonstrate the giant electronic transport anisotropy of the tellurene nanosheet.

We also calculated the charge density of the CBM and VBM along the *a*-axis and the *c*-axis, respectively, as demonstrated in Fig. 5c and Fig. S10.[†] Both the CBM and VBM's charge density show directional dependence, in other words, the partial charge density along the *a*-axis and the *c*-axis shows a giant difference in the level of overlap, clearly and visually suggesting the highly electronic anisotropy of tellurene.¹²

The carrier mobilities along the *a*-axis and *c*-axis are also calculated to further verify the electronic anisotropy of tellurene. As seen in Table 1, the hole mobility is one or two orders of magnitude higher than the electron mobility, demonstrating that the tellurene nanosheet exhibits p-type semiconductor characteristics.^{1,53} More importantly, the hole mobility along the *a*-axis is nearly two times that along the *c*-axis, confirming the giant electronic anisotropy in the tellurene nanosheet. The high mobility of hole μ_h along the *a*-axis is probably contributed from the delocalization of the lone-pair electrons of the tellurene nanosheet, which enhances the interchain binding (along the *a*-axis),^{38,54} and this metallic bonding becomes stronger in few-layered tellurene.³⁸

Table 1 The effective mass and the carrier mobility along the *a*-axis and *c*-axis of tellurene, where e, h, and 2D denote the electron, hole, and two-dimension, respectively

Direction	$m_e^* [m_0]^a$	$m_h^* [m_0]$	$C_{2D} [\text{J m}^{-2}]$	$E_{d, e} [\text{eV}]$	$E_{d, h} [\text{eV}]$	$\mu_{2D, e} [\text{cm}^2 \text{s}^{-1} \text{V}^{-1}]$	$\mu_{2D, h} [\text{cm}^2 \text{s}^{-1} \text{V}^{-1}]$
<i>a</i> -Axis	4.16	0.43	20.86	4.09 ± 0.267	1.14 ± 0.140	2.41–3.00 (2.68)	496.03–791.54 (625.16)
<i>c</i> -Axis	0.96	0.56	32.45	6.12 ± 0.272	3.26 ± 0.373	9.61–11.74 (10.59)	268.44–425.76 (338.32)

^a m_0 is the mass of the free electron, which is equal to 9.11×10^{-31} kg.

When the electromagnetic wave interacts with the solids, the dielectric polarization P occurs in the materials, which means that the positive and negative charges in materials are separated by the electric field component E of the electromagnetic wave. There are three types of dielectric polarizations, namely electric polarization, atomic polarization, and orientational polarization.¹⁹ Since the latter two types often take place in ionic crystals and molecules respectively, the dielectric polarization in the tellurene nanosheet can only be attributed to the electric polarization, which usually occurs in the UV-Visible region.¹⁹ In the electric polarization as illustrated in Fig. 5d, the electric field component of the electromagnetic wave distorts the positions of the negatively charged electrons and the positively charged nucleus in the opposite directions.⁵⁵ Therefore, the electrons' state of motion makes a great difference due to the electric polarization. The first-principles calculations indicate that the low-symmetry lattice structure of the tellurene nanosheet gives rise to the anisotropic carrier behaviours, such as the anisotropic effective mass and anisotropic carrier mobility, consequently causing the anisotropy in electric polarization. Therefore, the relationship between the dielectric polarization P and the electric field E for anisotropically electric polarization should be connected by the anisotropic dielectric functions, as given by⁵⁵

$$P_l = \epsilon_0(\epsilon_{lm} - 1)E_m \quad (l, m = x, y, z) \quad (6)$$

Herein, $\epsilon_0 = 8.854 \times 10^{-12} \text{ F m}^{-1}$ is the dielectric permittivity in free space, and ϵ_{lm} is the dielectric tensor. For a uniaxial crystal like tellurene, the dielectric tensor ϵ_{lm} is given in the form of eqn (4) with $\epsilon_{xx} = \epsilon_{yy} = \epsilon_0$ and $\epsilon_{zz} = \epsilon_e$. Hence, the anisotropy of electric polarization ultimately leads to the optical anisotropy with the connection of anisotropic dielectric functions.

Experimental section and methods

Material synthesis and characterization

The Te single crystal was purchased from SixCarbon Technology Shenzhen, and the tellurene nanosheet was synthesized by a solution method based on ref. 1. The thickness of the tellurene nanosheet was determined by atomic force microscopy (AFM, SPM9700, Shimadzu). A Raman system (LabRAM HR800, Horiba JobinYvon) was applied to confirm the low-symmetry lattice structure of the tellurene nanosheet and observe its highly in-plane anisotropic phenomena in optics. A commercial MMSE (ME-L, Wuhan E-optics

Technology Co. Ltd) and microscopic spectrophotometer (MSV-5200, JASCO) were respectively used to obtain azimuth-sensitive Mueller matrix off-diagonal elements spectra and polarization-resolved reflectance spectra. Imaging MMSE (NanoFilm_EP4, Accurion GmbH) was employed to obtain the spatially and spectrally resolved Mueller matrix of the tellurene nanosheet and further acquire its optical constant.

First-principles calculations

All the first-principles calculations were performed with the Vienna *ab initio* package (VASP)⁵⁶ by the projector augmented wave (PAW)⁵⁷ method based on density functional theory (DFT). The exchange–correlation energy was treated with generalized gradient approximation (GGA) using the Perdew–Burke–Ernzerhof (PBE) functional.⁵⁸ All the theoretical calculations included spin-orbit coupling (SOC) and the crystal structure was optimized under the consideration of vdW interactions of the optB88-vdW functional.⁵⁹ The cut-off energy for the plane-wave basis set was set to 300 eV for optical and electronic property calculations with the convergence criterion of total energy less than 10^{-5} eV. The electronic properties (bandstructure, partial charge density, and mobility) of tellurene were calculated from the stable structure of the two-layer (2L) nanosheet since the vdW interactions in monolayer tellurene are much strong, leading to structural phase transition.^{38,53} A vacuum layer of 15 Å was employed to avoid the interactions between the layers, and the crystal structure of 2L tellurene was optimized with the convergence criterion of 0.001 eV Å⁻¹ for forces. The bandstructure and mobility of 2L tellurene were examined based on the HSE06 hybrid functional⁶⁰ with a *k*-point mesh of $7 \times 5 \times 1$ in reciprocal space.

Carrier mobility calculations

The formula for calculating the carrier mobility μ_{2D} of 2D systems like tellurene is expressed as follows¹²

$$\mu_{2D,i,j} = \frac{e\hbar^3 C_{2D,j}}{k_B T m_{i,j}^* m_{DOS,i}^* E_{d,i,j}^2} \quad (i = e, h; j = a, c). \quad (7)$$

In eqn (7), e , \hbar , and k_B are the charge of electrons, reduced Planck constant ($\hbar = h/2\pi$, h is the Planck constant) and Boltzmann constant respectively. Room temperature, *i.e.*, $T = 300$ K, is used in the calculation. The density of state (DOS) effective mass $m_{DOS,i}$ for both the electron and hole in a 2D system is determined by

$$m_{DOS,i} = \sqrt{m_{i,a}^* m_{i,c}^*} \quad (i = e, h). \quad (8)$$

After the anisotropic correction, the μ_{2D} value along the a -axis can be approximated to⁶¹

$$\mu_{2D,i,a} \approx \frac{e\hbar^3 \left(\frac{5C_{2D,a} + 3C_{2D,c}}{8} \right)}{k_B T (m_{i,a}^*)^2 (m_{i,c}^*)^2 \left(\frac{9E_{d,i,a}^2 + 7E_{d,i,a}E_{d,i,c} + 4E_{d,i,c}^2}{20} \right)} (i = e, h), \quad (9)$$

and one can obtain the 2D mobility along the c -axis by simply interchanging subscript a with subscript c . $C_{2D,j}$ is the elastic modulus for a 2D system, which can be calculated by using the formula

$$C_{2D,j} = \frac{\partial^2 E_j}{\partial \left(\frac{\Delta l_j}{l_{0,j}} \right)^2} (j = a, c). \quad (10)$$

In eqn (10), E_j is the total energy under tiny compressive and tensile strain along the a -axis or c -axis and S_0 is the surface area of the equilibrium system; $l_{0,j}$ is the lattice constant of the a -axis or c -axis and Δl_j is the deformation of $l_{0,j}$ with a step of 0.5%. $E_{d,i,j}$ is the deformation potential constant of the CBM for the electron or the VBM for the hole along the a -axis or c -axis of tellurene, defined by the energy change $\Delta V_{i,j}$ of the CBM or VBM with respect to small strain along the a -axis or c -axis, *i.e.*,

$$E_{d,i,j} = \frac{\Delta V_{i,j}}{\Delta l_j} (i = e, h; j = a, c). \quad (11)$$

Here, energy change $\Delta V_{i,j}$ is required to deduct the energy level of vacuum for both the CBM and VBM when applying slight strain along the a -axis or c -axis. $E_{d,i,j}$ is equal to the slopes of the curves obtained by linearly fitting $\Delta V_{i,j}$ and $\Delta l_j/l_{0,j}$ (Fig. S11†).

Conclusions

In summary, the giant in-plane optical anisotropies of tellurene are quantitatively evaluated with accurate and reliable optical functions, including the complex refractive indices and dielectric functions, determined by high-resolution imaging MMSE. In addition, the giant birefringence ($|\Delta n|_{max} = 0.48$) and dichroism ($\Delta k > 0.4$) derived from the optical functions indicate that tellurene is a promising candidate for designing polarization-sensitive optoelectronic devices. We find from the dielectric functions that tellurene exhibits metalloid behavior, which originates from the delocalization of Te lone-pair electrons. The first-principles calculated anisotropic effective mass and carrier mobility, with significant differences along the a -axis and the c -axis, as well as the anisotropic partial charge density demonstrate the strong in-plane electronic anisotropy of tellurene, which bridges tellurene's low-symmetry lattice structure with optical anisotropies to further reveal the physical origin of the optical anisotropy. The giant electronic an-

isotropy, resulting from tellurene's low-symmetry lattice structure, leads to anisotropically electric polarization and ultimately giant optical anisotropy. The proposed results and discussions can help to deeply and comprehensively understand the relationship between the lattice structure and the optical anisotropy in tellurene. This paper provides a general and quantitative way to explore the optical anisotropies of novel low-symmetry materials, and will further guide the optimal design of related optoelectronic devices.

Conflicts of interest

There are no conflicts to declare.

Acknowledgements

This work is funded by the National Natural Science Foundation of China (51727809, 51805193, 52130504, and 61974050); the Fundamental Research Funds for the Central Universities (2021XXJS113); the Key Research and Development Plan of Hubei Province (2021BAA013); and the Natural Science Foundation of Hubei Province (2021CFB322). The authors are thankful for the facility support of the Center of Optoelectronic Micro & Nano Fabrication and Characterizing Facility of Wuhan National Laboratory for Optoelectronics (WNLO) of Huazhong University of Science and Technology (HUST), the Experiment Center for Advanced Manufacturing and Technology in School of Mechanical Science & Engineering of HUST, and the Analysis and Testing Center of HUST.

References

- Y. Wang, G. Qiu, R. Wang, S. Huang, Q. Wang, Y. Liu, Y. Du, W. A. Goddard, M. J. Kim, X. Xu, P. D. Ye and W. Wu, *Nat. Electron.*, 2018, **1**, 228–236.
- L. Tong, X. Huang, P. Wang, L. Ye, M. Peng, L. An, Q. Sun, Y. Zhang, G. Yang, Z. Li, F. Zhong, F. Wang, Y. Wang, M. Motlag, W. Wu, G. J. Cheng and W. Hu, *Nat. Commun.*, 2020, **11**, 2308.
- X. Huang, J. Guan, Z. Lin, B. Liu, S. Xing, W. Wang and J. Guo, *Nano Lett.*, 2017, **17**, 4619–4623.
- A. Londoño-Calderon, D. J. Williams, M. M. Schneider, B. H. Savitzky, C. Ophus, S. Ma, H. Zhu and M. T. Pettes, *Nanoscale*, 2021, **13**, 9606–9614.
- F. Calavalle, M. Suárez-Rodríguez, B. Martín-García, A. Johansson, D. C. Vaz, H. Yang, I. V. Maznichenko, S. Ostanin, A. Mateo-Alonso, A. Chuvalin, I. Mertig, M. Gobbi, F. Casanova and L. E. Hueso, *Nat. Mater.*, 2022, **21**, 526–532.
- G. Qiu, C. Niu, Y. Wang, M. Si, Z. Zhang, W. Wu and P. D. Ye, *Nat. Nanotechnol.*, 2020, **15**, 585–591.
- A. K. Tareen, K. Khan, M. Aslam, H. Zhang and X. Liu, *Nanoscale*, 2021, **13**, 510–552.

- 8 B. Song, H. Gu, S. Zhu, H. Jiang, X. Chen, C. Zhang and S. Liu, *Appl. Surf. Sci.*, 2018, **439**, 1079–1087.
- 9 G. A. Ermolaev, D. V. Grudinin, Y. V. Stebunov, K. V. Voronin, V. G. Kravets, J. Duan, A. B. Mazitov, G. I. Tselikov, A. Bylinkin, D. I. Yakubovsky, S. M. Novikov, D. G. Baranov, A. Y. Nikitin, I. A. Kruglov, T. Shegai, P. Alonso-González, A. N. Grigorenko, A. V. Arsenin, K. S. Novoselov and V. S. Volkov, *Nat. Commun.*, 2021, **12**, 854.
- 10 A. Segura, L. Artús, R. Cuscó, T. Taniguchi, G. Cassabois and B. Gil, *Phys. Rev. Mater.*, 2018, **2**, 024001.
- 11 M. Amani, C. Tan, G. Zhang, C. Zhao, J. Bullock, X. Song, H. Kim, V. R. Shrestha, Y. Gao, K. B. Crozier, M. Scott and A. Javey, *ACS Nano*, 2018, **12**, 7253–7263.
- 12 J. Qiao, X. Kong, Z.-X. Hu, F. Yang and W. Ji, *Nat. Commun.*, 2014, **5**, 4475.
- 13 S. Niu, G. Joe, H. Zhao, Y. Zhou, T. Orvis, H. Huyan, J. Salman, K. Mahalingam, B. Urwin, J. Wu, Y. Liu, T. E. Tiwald, S. B. Cronin, B. M. Howe, M. Mecklenburg, R. Haiges, D. J. Singh, H. Wang, M. A. Kats and J. Ravichandran, *Nat. Photonics*, 2018, **12**, 392–396.
- 14 Y. Liu, M. Wu, Z. Sun, S. Yang, C. Hu, L. Huang, W. Shen, B. Wei, Z. Wang, S. Yang, Y. Ye, Y. Li and C. Jiang, *Nanoscale*, 2019, **11**, 23116–23125.
- 15 W. Shen, C. Hu, J. Tao, J. Liu, S. Fan, Y. Wei, C. An, J. Chen, S. Wu, Y. Li, J. Liu, D. Zhang, L. Sun and X. Hu, *Nanoscale*, 2018, **10**, 8329–8337.
- 16 Y. Xu, Z. Shi, X. Shi, K. Zhang and H. Zhang, *Nanoscale*, 2019, **11**, 14491–14527.
- 17 X. Li, H. Liu, C. Ke, W. Tang, M. Liu, F. Huang, Y. Wu, Z. Wu and J. Kang, *Laser Photonics Rev.*, 2021, **15**, 2100322.
- 18 M. Brinkmann, J. Hayden, M. Letz, S. Reichel, C. Click, W. Mannstadt, B. Schreder, S. Wolff, S. Ritter, M. J. Davis, T. E. Bauer, H. Ren, Y.-H. Fan, Y. Menke, S.-T. Wu, K. Bonrad, E. Krätzig, K. Buse and R. A. Paquin, in *Springer handbook of lasers and optics*, ed. F. Träger, Springer Berlin Heidelberg, Berlin, Heidelberg, 2012, pp. 253–399.
- 19 H. Fujiwara, *Spectroscopic ellipsometry: principles and applications*, John Wiley & Sons, Chichester, England, 2007.
- 20 M. Steger, S. M. Janke, P. C. Sercel, B. W. Larson, H. Lu, X. Qin, V. W.-Z. Yu, V. Blum and J. L. Blackburn, *Nanoscale*, 2022, **14**, 752–765.
- 21 B. Song, H. Gu, M. Fang, X. Chen, H. Jiang, R. Wang, T. Zhai, Y.-T. Ho and S. Liu, *Adv. Opt. Mater.*, 2019, **7**, 1801250.
- 22 M. Fang, Z. Wang, H. Gu, M. Tong, B. Song, X. Xie, T. Zhou, X. Chen, H. Jiang, T. Jiang and S. Liu, *Appl. Surf. Sci.*, 2020, **509**, 144822.
- 23 E. Barré, O. Karni, E. Liu, A. L. O’Beirne, X. Chen, H. B. Ribeiro, L. Yu, B. Kim, K. Watanabe, T. Taniguchi, K. Barmak, C. H. Lui, S. Refaelly-Abramson, F. H. D. Jornada and T. F. Heinz, *Science*, 2022, **376**, 406–410.
- 24 H. Gu, B. Song, M. Fang, Y. Hong, X. Chen, H. Jiang, W. Ren and S. Liu, *Nanoscale*, 2019, **11**, 22762–22771.
- 25 A. V. Hippel, *J. Chem. Phys.*, 1948, **16**, 372–380.
- 26 X. Li, L. Tao, Z. Chen, H. Fang, X. Li, X. Wang, J.-B. Xu and H. Zhu, *Appl. Phys. Rev.*, 2017, **4**, 021306.
- 27 Y. Du, G. Qiu, Y. Wang, M. Si, X. Xu, W. Wu and P. D. Ye, *Nano Lett.*, 2017, **17**, 3965–3973.
- 28 X. Zhang, J. Jiang, A. A. Suleiman, B. Jin, X. Hu, X. Zhou and T. Zhai, *Adv. Funct. Mater.*, 2019, **29**, 1906585.
- 29 R. M. Martin, G. Lucovsky and K. Helliwell, *Phys. Rev. B: Solid State*, 1976, **13**, 1383–1395.
- 30 Z. Guo, H. Gu, M. Fang, B. Song, W. Wang, X. Chen, C. Zhang, H. Jiang, L. Wang and S. Liu, *ACS Mater. Lett.*, 2021, **3**, 525–534.
- 31 Y. Yang, N. Akozbek, T.-H. Kim, J. M. Sanz, F. Moreno, M. Losurdo, A. S. Brown and H. O. Everitt, *ACS Photonics*, 2014, **1**, 582–589.
- 32 X. Zhang, Q.-H. Tan, J.-B. Wu, W. Shi and P.-H. Tan, *Nanoscale*, 2016, **8**, 6435–6450.
- 33 X.-L. Liu, X. Zhang, M.-L. Lin and P.-H. Tan, *Chin. Phys. B*, 2017, **26**, 067802.
- 34 P. S. Hauge, *Surf. Sci.*, 1980, **96**, 108–140.
- 35 S. Funke, M. Duwe, F. Balzer, P. H. Thiesen, K. Hingerl and M. Schiek, *J. Phys. Chem. Lett.*, 2021, **12**, 3053–3058.
- 36 K. Locharoenrat, *Optical properties of solids: an introductory textbook*, CRC Press, New York, 1st edn, 2016.
- 37 D. Medina-Cruz, W. Tien-Street, A. Vernet-Crua, B. Zhang, X. Huang, A. Murali, J. Chen, Y. Liu, J. M. Garcia-Martin, J. L. Cholula-Díaz and T. Webster, in *Racing for the surface: antimicrobial and interface tissue engineering*, ed. B. Li, T. F. Moriarty, T. Webster and M. Xing, Springer International Publishing, Cham, 2020, ch. 26, pp. 723–783.
- 38 Y. Liu, W. Wu and W. A. Goddard, *J. Am. Chem. Soc.*, 2018, **140**, 550–553.
- 39 G. Ghosh, *Opt. Commun.*, 1999, **163**, 95–102.
- 40 M. J. Dodge, *Appl. Opt.*, 1984, **23**, 1980–1985.
- 41 S.-Y. Lee and K.-J. Yee, *2D Mater.*, 2021, **9**, 015020.
- 42 N. Papadopoulos, R. Frisenda, R. Biele, E. Flores, J. R. Ares, C. Sánchez, H. S. J. van der Zant, I. J. Ferrer, R. D’Agosta and A. Castellanos-Gomez, *Nanoscale*, 2018, **10**, 12424–12429.
- 43 C. Wu, T. Wu, X. Jiang, Z. Wang, H. Sha, L. Lin, Z. Lin, Z. Huang, X. Long, M. G. Humphrey and C. Zhang, *J. Am. Chem. Soc.*, 2021, **143**, 4138–4142.
- 44 S. Liu, X. Liu, S. Zhao, Y. Liu, L. Li, Q. Ding, Y. Li, Z. Lin, J. Luo and M. Hong, *Angew. Chem., Int. Ed.*, 2020, **59**, 9414–9417.
- 45 H. Yang, H. Jussila, A. Autere, H.-P. Komsa, G. Ye, X. Chen, T. Hasan and Z. Sun, *ACS Photonics*, 2017, **4**, 3023–3030.
- 46 X. Chen, W.-G. Lu, J. Tang, Y. Zhang, Y. Wang, G. D. Scholes and H. Zhong, *Nat. Photonics*, 2021, **15**, 813–816.
- 47 X. Wang, Y. Li, L. Huang, X.-W. Jiang, L. Jiang, H. Dong, Z. Wei, J. Li and W. Hu, *J. Am. Chem. Soc.*, 2017, **139**, 14976–14982.
- 48 J. Wang, C. Jiang, W. Li and X. Xiao, *Adv. Opt. Mater.*, 2022, **10**, 2102436.
- 49 D. Andres-Penares, M. Brotons-Gisbert, C. Bonato, J. F. Sánchez-Royo and B. D. Gerardot, *Appl. Phys. Lett.*, 2021, **119**, 223104.

- 50 A. J. Mannix, X.-F. Zhou, B. Kiraly, J. D. Wood, D. Alducin, B. D. Myers, X. Liu, B. L. Fisher, U. Santiago, J. R. Guest, M. J. Yacaman, A. Ponce, A. R. Oganov, M. C. Hersam and N. P. Guisinger, *Science*, 2015, **350**, 1513–1516.
- 51 Y. Yang, S.-C. Liu, Y. Wang, M. Long, C.-M. Dai, S. Chen, B. Zhang, Z. Sun, Z. Sun, C. Hu, S. Zhang, L. Tong, G. Zhang, D.-J. Xue and J.-S. Hu, *Adv. Opt. Mater.*, 2019, **7**, 1801311.
- 52 L. D. Whalley, J. M. Frost, B. J. Morgan and A. Walsh, *Phys. Rev. B*, 2019, **99**, 085207.
- 53 J. Qiao, Y. Pan, F. Yang, C. Wang, Y. Chai and W. Ji, *Sci. Bull.*, 2018, **63**, 159–168.
- 54 S. Yi, Z. Zhu, X. Cai, Y. Jia and J.-H. Cho, *Inorg. Chem.*, 2018, **57**, 5083–5088.
- 55 V. Raicu and Y. Feldman, *Dielectric Relaxation in Biological Systems: Physical Principles, Methods, and Applications*, OUP Oxford, 2015.
- 56 G. Kresse and J. Furthmüller, *Comput. Mater. Sci.*, 1996, **6**, 15–50.
- 57 P. E. Blöchl, *Phys. Rev. B: Condens. Matter Mater. Phys.*, 1994, **50**, 17953–17979.
- 58 J. P. Perdew, K. Burke and M. Ernzerhof, *Phys. Rev. Lett.*, 1996, **77**, 3865–3868.
- 59 J. Klimeš, D. R. Bowler and A. Michaelides, *J. Phys.: Condens. Matter*, 2009, **22**, 022201.
- 60 J. Heyd, G. E. Scuseria and M. Ernzerhof, *J. Chem. Phys.*, 2003, **118**, 8207–8215.
- 61 H. Lang, S. Zhang and Z. Liu, *Phys. Rev. B*, 2016, **94**, 235306.

Supporting Information

Giant in-plane optical and electronic anisotropy in tellurene: A quantitative exploration

Zhengfeng Guo,^{ab} Honggang Gu,^{*ad} Mingsheng Fang,^a Lei Ye^c and Shiyuan Liu^{*acd}

^a*State Key Laboratory of Digital Manufacturing Equipment and Technology, Huazhong University of Science and Technology, Wuhan 430074, China*

^b*Innovation Institute, Huazhong University of Science and Technology, Wuhan 430074, China*

^c*School of Optical and Electronic Information, Huazhong University of Science and Technology, Wuhan 430074, China*

^d*Optics Valley Laboratory, Wuhan 430074, China*

*Corresponding E-mails:

hongganggu@hust.edu.cn (H. Gu); shyliu@hust.edu.cn (S. Liu).

Supporting Note S1. Theoretical calculating peak intensities of the Raman modes

The theoretical peak intensities of the Raman modes are calculated to fit the experimental ones. The peak intensity I of each Raman mode can be calculated by the formula^{S1, 2}

$$I \propto |\mathbf{e}_{\text{out}} \cdot \mathbf{R} \cdot \mathbf{e}_{\text{in}}|^2, \quad (\text{S1})$$

where, \mathbf{e}_{out} and \mathbf{e}_{in} are respectively the unit polarization vectors of the scattered Raman signal and the incident laser. After the incident laser goes through the polarizer, its electric field direction is parallel to the z -axis of the Raman laboratory coordinates, and $\mathbf{e}_{\text{in}} = [0, 0, 1]^T$. Since the analyzer is parallel to the polarizer (Fig. S3), we have $\mathbf{e}_{\text{out}} = [0, 0, 1]$. \mathbf{R} is the Raman tensor for each Raman mode. Tellurene belongs to the D_3^4 space group^{S3}, and therefore the Raman tensors for A_1 , E_1 -TO, and E_2 are respectively given by^{S4}

$$\mathbf{R}_{A_1} = \begin{bmatrix} a & 0 & 0 \\ 0 & a & 0 \\ 0 & 0 & b \end{bmatrix}, \quad (\text{S2a})$$

$$\mathbf{R}_{E_1\text{-TO}} = \begin{bmatrix} c & 0 & 0 \\ 0 & -c & d \\ 0 & d & 0 \end{bmatrix}, \quad (\text{S2b})$$

and

$$\mathbf{R}_{E_2} = \begin{bmatrix} 0 & -c & -d \\ -c & 0 & 0 \\ -d & 0 & 0 \end{bmatrix}. \quad (\text{S2c})$$

The Raman tensors are defined with respect to the crystal coordinates. Therefore, the coordinate conversion must be taken into account due to the azimuth rotation of the sample in the Raman measurements. The Raman tensors after the coordinate conversion \mathbf{R}' can be written as^{S1}

$$\mathbf{R}' = \mathbf{A}^T \mathbf{R} \mathbf{A}, \quad (\text{S3a})$$

where, \mathbf{A} is the rotation matrix

$$\mathbf{A} = \begin{bmatrix} \cos(\theta + \alpha) & 0 & \sin(\theta + \alpha) \\ 0 & 1 & 0 \\ -\sin(\theta + \alpha) & 0 & \cos(\theta + \alpha) \end{bmatrix}, \quad (\text{S3b})$$

and \mathbf{A}^T is the transposed matrix of \mathbf{A} . Herein, θ is the angle between the z -axis and the c -axis of the tellurene nanosheet, and α is the rotation angle, as shown in Fig. S4.

According to the above derivation, the peak intensity of the Raman mode in our measurement configuration can be described as

$$I \propto |\mathbf{e}_{\text{out}} \cdot \mathbf{R} \cdot \mathbf{e}_{\text{in}}|^2 = |\mathbf{e}_{\text{out}} \cdot \mathbf{A}^T \mathbf{R} \mathbf{A} \cdot \mathbf{e}_{\text{in}}|^2. \quad (\text{S4a})$$

Ultimately, the peak intensities of A_1 , E_1 -TO, and E_2 Raman modes are respectively given by

$$I_{A_1} \propto |a \sin^2(\theta + \alpha) + b \cos^2(\theta + \alpha)|^2, \quad (\text{S4b})$$

$$I_{E_1\text{-TO}} \propto |c \sin^2(\theta + \alpha)|^2, \quad (\text{S4c})$$

and

$$I_{E_2} \propto |-2d \sin(\theta + \alpha) \cos(\theta + \alpha)|^2 = |d \sin 2(\theta + \alpha)|^2. \quad (\text{S4e})$$

Here, θ is 90° , which means z -axis and c -axis is perpendicular to each other at the initial Raman measurement.

Supporting Note S2. Imaging Mueller matrix spectroscopic ellipsometry analysis

The constructed stacking model is composed of the geometric structure and the dielectric function for each part of geometric construction. The tellurene nanosheet and Si substrate with SiO_2 oxide layer consist of the multilayer film structure. The structure parameters for this multilayer film structure are the thickness of each layer. Besides, on account of smooth surface of tellurene nanosheet measured by AFM in Fig. S7, the roughness of tellurene nanosheet or overlay model (such as effective medium approximation, EMA^{S5}) are not taken into consideration. Since more attention is paid to the layer of tellurene nanosheet, the thickness and the dielectric function of Si substrate with SiO_2 oxide layer were predetermined with a separate reference measurement on an uncoated region before determining those of tellurene nanosheet.

To acquire the thickness and the dielectric function of tellurene nanosheet, the cubic-

spline functions^{S6} vertical and parallel to the optics axis were applied and adjusted to obtain the best match with experimental data. Owing to the fact that the cubic-spline functions are not satisfied with Kramers-Kronig consistency^{S7}, the cubic-spline functions are lack of direct physical meaning. In consequence, the Lorentz oscillator model (with physical implication) along and vertical to the optics axis was introduced to fit Mueller matrix spectra, which is expressed as the sum form of several Lorentz oscillators^{S8, 9}

$$\varepsilon(E) = \sum_q^Q \varepsilon_{\text{Lorentz}}^q(E_{0,q}, A_q, \Gamma_q; E) = \sum_q^Q \frac{E_{0,q} A_q}{E_{0,q}^2 - E^2 + i\Gamma_q E}. \quad (\text{S5})$$

In Equation S1, E is the photon energy with the unit of eV, and the Q is the total number of Lorentz oscillators. In addition, $E_{0,q}$, A_q , and Γ_q are the q th oscillator's center energy, strength (amplitude), and damping coefficient respectively.

In our ellipsometric analysis, both two Lorentz oscillators were employed along and vertical to the optics axis, whose best fitted parameters are summarized in Table S1.

Besides, the extracted thickness of the tellurene nanosheet is 71.0 nm in perfect accordance with the AFM value 72.6 nm as shown in Fig. S6, further implying the reliability and accuracy of the ellipsometric analysis.

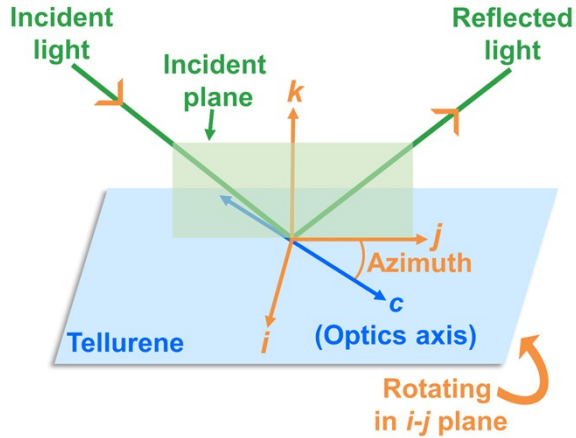


Fig. S1 The ellipsometric measurement schematic diagram of tellurium (Te), where the azimuth is defined as the angle between *c*-axis of Te and *j*-axis of ellipsometric coordinate (*i-j-k*).

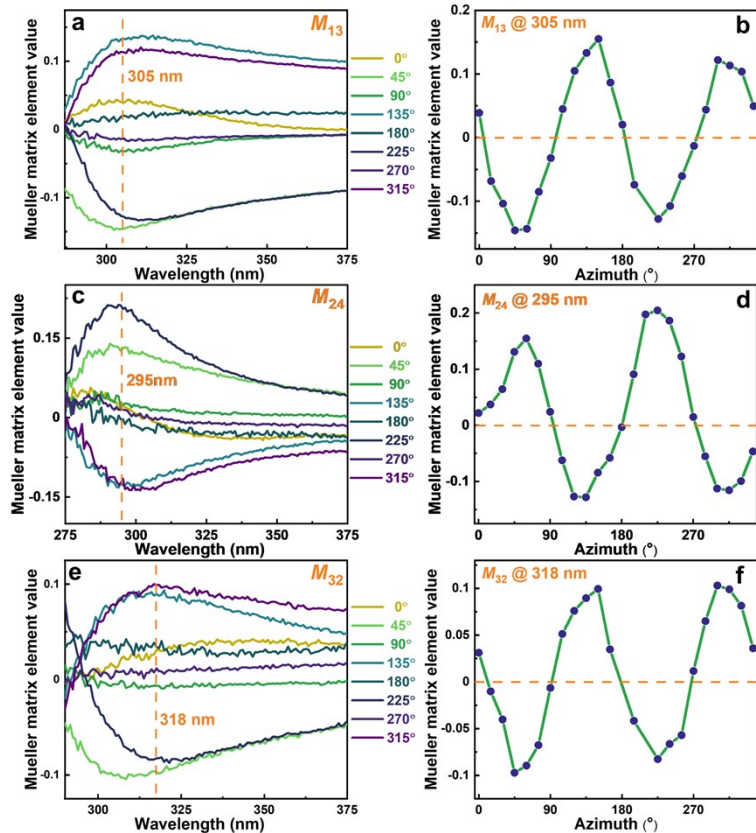


Fig. S2 The other representative azimuth-sensitive off-diagonal Mueller matrix elements (M_{13} , M_{24} , and M_{32}) spectra at varied azimuths and incident angle θ_i of 65° (a, c, and e) and those at the selected wavelength (b, d, and f).

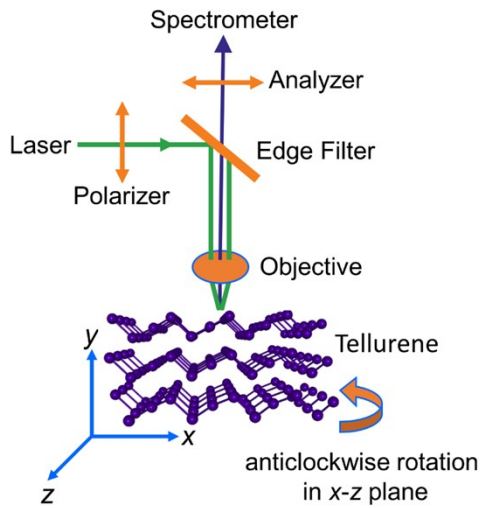


Fig. S3 Schematic diagram of the Raman system configuration, where the polarizer and analyzer are parallel to each other and the tellurene is anticlockwise rotated in x - z plane.

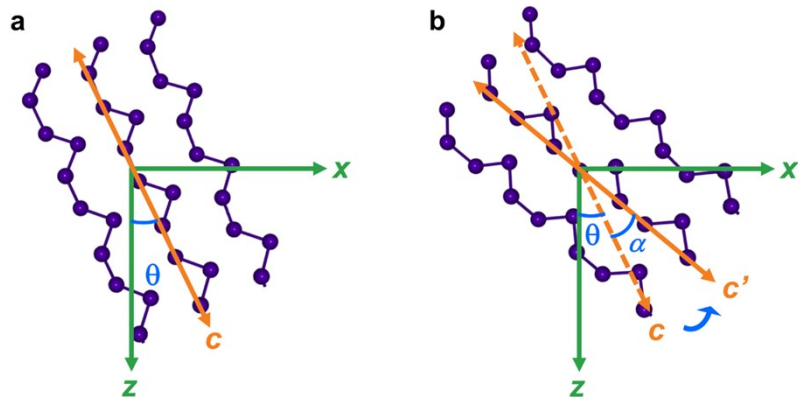


Fig. S4 The tellurene in x - z plane of Raman coordinate (x - y - z) at the beginning of Raman measurement (a) and after anticlockwise rotating α° (b).

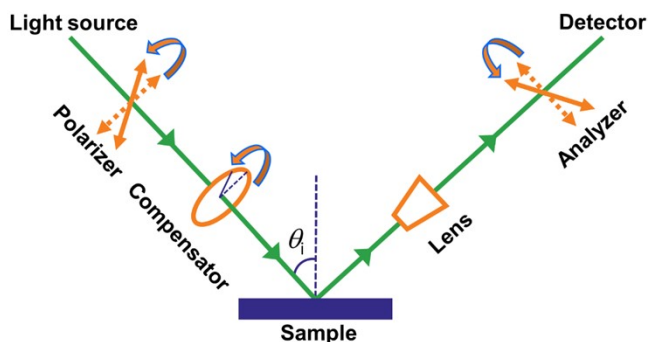


Fig. S5 The working principle of the imaging Mueller matrix spectroscopic ellipsometry (MMSE), where θ_i represents the incident angle and the polarizer, compensator and analyzer are rotatable to obtain the first three row of Mueller matrix and high spatial contrast of sample^{88, 10}. Combined with microscopic imaging system,

the lateral resolution of the imaging MMSE can even reach up to 2 μm ^{S6}.

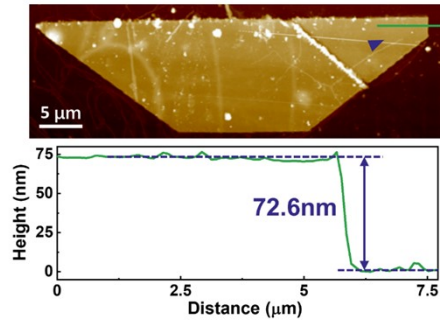


Fig. S6 The atomic force microscopy (AFM) image of the same tellurene nanosheet measured by the imaging MMSE, where the triangle is the region to extract the Mueller matrix spectra for the spectroscopic analysis.

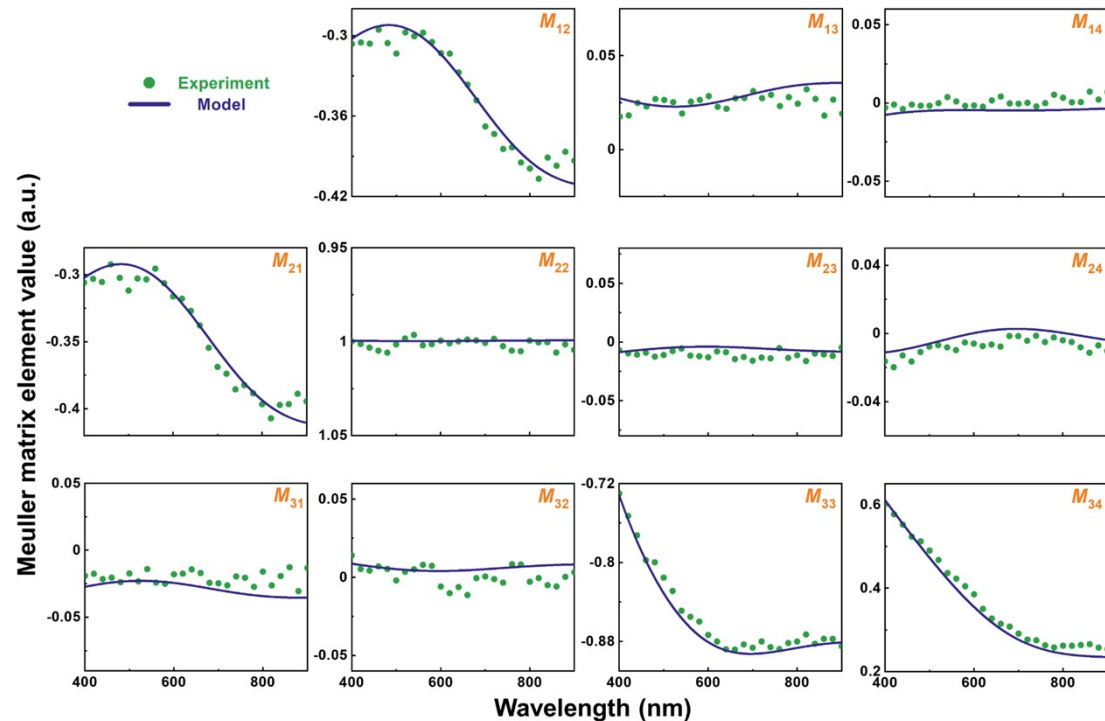


Fig. S7 The experimental (green points) and model-calculated (solid line) Mueller matrix spectra at the incident angle of 50°.

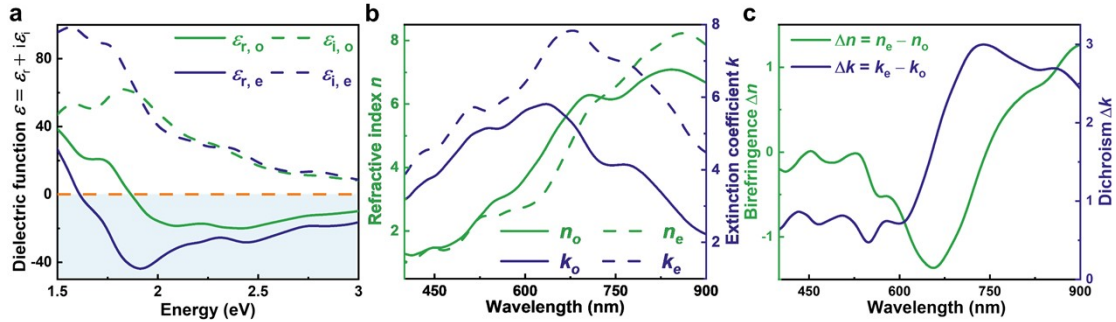


Fig. S8 The first-principle calculated dielectric function spectra (a), complex refractive index spectra (b), and in-plane birefringence Δn ($= n_e - n_o$) and dichroism Δk ($= k_e - k_o$).

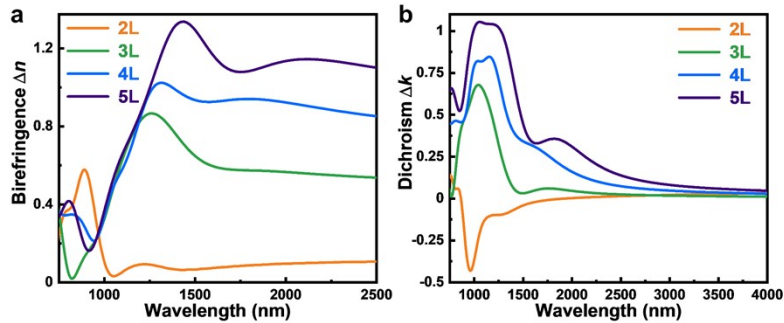


Fig. S9 The first-principle calculated tellurene's thickness dependence of birefringence Δn (a) and dichroism Δk (b), where "L" denotes layers.

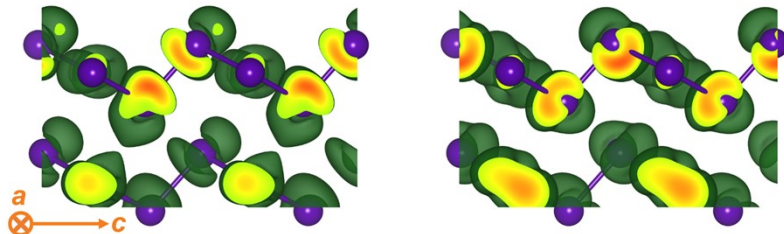


Fig. S10 The charge density of conduction band maximum (CBM) using an isosurface of 0.3 me\AA^{-3} , left: along the a -axis, right: along the c -axis

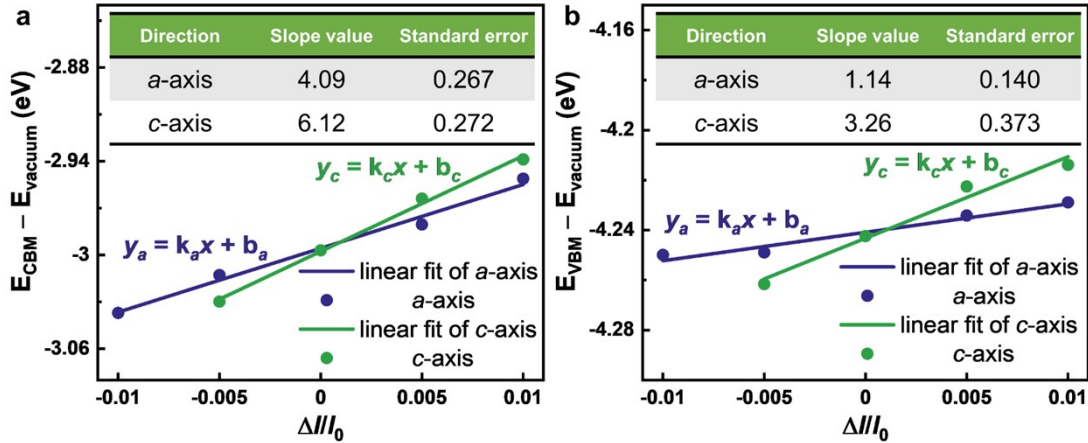


Fig. S11 The relationship between conduction band minimum (CBM, a) or valence band maximum (VBM, b), deducting the vacuum energy level E_{vacuum} , and deformation of lattice constant (a -axis or c -axis) $\Delta l_j/l_{0,j}$ ($j = a, c$) with their linearly fit, where the insert tables are the slopes and its standard errors of these linearly fitted lines. As -0.01 strain (compressive strain) along c -axis causes great fluctuation in linearly fitting, it is excluded from linearly fit.

Table S1. The best fitted parameters of Lorentz oscillators model used in uniaxial anisotropic model of tellurene nanosheet.

	Center energy (E_0) [eV]	Amplitude (A) [(eV) 2]	Damping coefficient (I) [eV]
ε_0	1.10 ± 0.172	33.84 ± 16.178	1.59 ± 0.152
	1.61 ± 0.060	36.26 ± 15.737	1.36 ± 0.127
ε_e	1.08 ± 0.221	51.38 ± 2.724	5.79 ± 0.775
	1.85 ± 0.007	29.76 ± 1.970	1.22 ± 0.039

Table S2. Comparison of birefringence in commercial birefringent materials, typical low-dimensional materials, and well-designed birefringent materials.

Materials	Birefringence (Δn)	Reference s
Tellurene	0.48	This work
Quartz (SiO_2)	0.009	Ref S11
MgF_2	0.012	Ref S12
Calcite (CaCO_3)	0.20	Ref S11
Black phosphorus (BP)	0.15	Ref S13
TiS_3	0.30 ± 0.04	Ref S14
BaTiS_3	0.76	Ref S15
h-BN ^a	0.3 in vis-near infrared region 2 in UV region	Ref S16, 17
$\alpha\text{-MoO}_3$	0.11	Ref S18
MoS_2^{a}	1.5 in near infrared region 3 in visible range	Ref S19
Cs_4PbBr_6 perovskite crystals embedded with CsPbBr_3 nanocrystals	0.018	Ref S20
$\text{CeF}_2(\text{SO}_4)$	0.36	Ref S21
$\text{Rb}_2\text{VO}(\text{O}_2)_2\text{F}$	0.19	Ref S22
$[\text{Al}(\text{H}_2\text{O})_6](\text{IO}_3)_2(\text{NO}_3)$	0.252	Ref S23

^a although the birefringences of h-BN and MoS_2 are rather larger than many other materials, they are out-of-plane rather than more accessible in-plane birefringence like tellurene.

References

- S1. X.-L. Liu, X. Zhang, M.-L. Lin and P.-H. Tan, *Chin. Phys. B*, 2017, **26**, 067802.
- S2. M. A. Pimenta, G. C. Resende, H. B. Ribeiro and B. R. Carvalho, *Phys. Chem. Chem. Phys.*, 2021, **23**, 27103-27123.
- S3. L. Tong, X. Huang, P. Wang, L. Ye, M. Peng, L. An, Q. Sun, Y. Zhang, G. Yang, Z. Li, F. Zhong, F. Wang, Y. Wang, M. Motlag, W. Wu, G. J. Cheng and W. Hu, *Nat. Commun.*, 2020, **11**, 2308.
- S4. E. Anastassakis and M. Cardona, *Phys. Status Solidi B*, 1981, **104**, 589-600.
- S5. P. Petrik, M. Fried, T. Lohner, R. Berger, L. P. Biró, C. Schneider, J. Gyulai and H. Ryssel, *Thin Solid Films*, 1998, **313-314**, 259-263.
- S6. S. Funke, M. Duwe, F. Balzer, P. H. Thiesen, K. Hingerl and M. Schiek, *J. Phys. Chem. Lett.*, 2021, **12**, 3053-3058.
- S7. B. Su, Y. Song, Y. Hou, X. Chen, J. Zhao, Y. Ma, Y. Yang, J. Guo, J. Luo and Z.-G. Chen, *Adv. Mater.*, 2019, **31**, 1903498.
- S8. H. Fujiwara, *Spectroscopic ellipsometry: principles and applications*, John Wiley & Sons, Chichester, England, 2007.
- S9. Z. Guo, H. Gu, M. Fang, B. Song, W. Wang, X. Chen, C. Zhang, H. Jiang, L. Wang and S. Liu, *ACS Mater. Lett.*, 2021, **3**, 525-534.
- S10. P. S. Hauge, *Surf. Sci.*, 1980, **96**, 108-140.
- S11. G. Ghosh, *Opt. Commun.*, 1999, **163**, 95-102.
- S12. M. J. Dodge, *Appl. Opt.*, 1984, **23**, 1980-1985.
- S13. S.-Y. Lee and K.-J. Yee, *2D Mater.*, 2021, **9**, 015020.
- S14. N. Papadopoulos, R. Frisenda, R. Biele, E. Flores, J. R. Ares, C. Sánchez, H. S. J. van der Zant, I. J. Ferrer, R. D'Agosta and A. Castellanos-Gomez, *Nanoscale*, 2018, **10**, 12424-12429.
- S15. S. Niu, G. Joe, H. Zhao, Y. Zhou, T. Orvis, H. Huyan, J. Salman, K. Mahalingam, B. Urwin, J. Wu, Y. Liu, T. E. Tiwald, S. B. Cronin, B. M. Howe, M. Mecklenburg, R. Haiges, D. J. Singh, H. Wang, M. A. Kats and J. Ravichandran, *Nat. Photonics*, 2018, **12**, 392-396.
- S16. Y. Rah, Y. Jin, S. Kim and K. Yu, *Opt. Lett.*, 2019, **44**, 3797-3800.
- S17. A. Segura, L. Artús, R. Cuscó, T. Taniguchi, G. Cassabois and B. Gil, *Phys. Rev. Mater.*, 2018, **2**, 024001.
- S18. D. Andres-Penares, M. Brotons-Gisbert, C. Bonato, J. F. Sánchez-Royo and B. D. Gerardot, *Appl. Phys. Lett.*, 2021, **119**, 223104.
- S19. G. A. Ermolaev, D. V. Grudinin, Y. V. Stebunov, K. V. Voronin, V. G. Kravets, J. Duan, A. B. Mazitov, G. I. Tselikov, A. Bylinkin, D. I. Yakubovsky, S. M. Novikov, D. G. Baranov, A. Y. Nikitin, I. A. Kruglov, T. Shegai, P. Alonso-González, A. N. Grigorenko, A. V. Arsenin, K. S. Novoselov and V. S. Volkov, *Nat. Commun.*, 2021, **12**, 854.
- S20. X. Chen, W.-g. Lu, J. Tang, Y. Zhang, Y. Wang, G. D. Scholes and H. Zhong, *Nat. Photonics*, 2021, **15**, 813–816.
- S21. C. Wu, T. Wu, X. Jiang, Z. Wang, H. Sha, L. Lin, Z. Lin, Z. Huang, X. Long, M. G. Humphrey and C. Zhang, *J. Am. Chem. Soc.*, 2021, **143**, 4138-4142.
- S22. S. Liu, X. Liu, S. Zhao, Y. Liu, L. Li, Q. Ding, Y. Li, Z. Lin, J. Luo and M. Hong,

- Angew. Chem., Int. Ed.*, 2020, **59**, 9414-9417.
- S23. Z. Bai, C.-L. Hu, D. Wang, L. Liu, L. Zhang, Y. Huang, F. Yuan and Z. Lin, *Chem. Commun.*, 2020, **56**, 11629-11632.